International Journal of Multiphase Flow 36 (2010) 503–512

Contents lists available at ScienceDirect

International Journal of Multiphase Flow

journal homepage: www.elsevier.com/locate/ijmulflow

Brief Communication

Flow around a contaminated fluid sphere

A. Saboni *, S. Alexandrova, M. Mory

Laboratoire de Thermique, Energétique et Procédés UPPA, Avenue de l'Université, 64000 Pau, France

ARTICLE INFO

Article history:
Received 11 October 2009
Received in revised form 13 January 2010
Accepted 19 January 2010
Available online 2 February 2010

Keywords:
Fluid sphere
Flow
Viscosity ratio
Interface contamination

1. Introduction

It has long been observed that interface contamination modifies flow around bubbles or drops in relative motion inside a fluid. The so-called stagnant-cap model (Griffith, 1962) has been widely used to describe flow around contaminated bubbles. It assumes that surface active agents tend to accumulate at the rear of the bubble, forming a cap with an immobile surface, while the rest of the bubble surface remains mobile (Fig. 1). The magnitude of contamination is described by the polar angle θ_{cap} of the spherical coordinate system having the z axis coinciding with the direction of the relative motion of the bubble or drop in the fluid. This model is in agreement with experimental observations of several authors (Savic, 1953; Garner and Skelland, 1955; Elzinga and Banchero; 1961; Griffith 1962; Horton et al., 1965; Huang and Kintner, 1969; Beitel and Heideger, 1971) who found the formation of a stagnant cap at the rear of a drop or a bubble contaminated with slightly soluble surfactant (high Peclet number). The case of creeping flow (Stokes flow) past bubbles with stagnant cap has been investigated by several authors (Savic, 1953; Davis and Acrivos, 1966; Harper, 1973, 1982). The problem was generalized by Sadhal and Johnson (1983) to include both drops and bubbles. In their study, steady creeping flow past a viscous fluid sphere partially coated with thin films was examined analytically. The solution yields the following expression for the drag coefficient of a viscous fluid sphere:

$$C_D = \frac{16}{\mathrm{Re}}\left\{\frac{1}{2\pi(1+\kappa)}\left(2(\pi-\theta_{cap})+\sin(\theta_{cap})+\sin(2\theta_{cap})-\frac{1}{3}\sin(3\theta_{cap})\right)+\frac{2+3\kappa}{2+2\kappa}\right\}, \quad (1)$$

It is defined from the force component F_D applied on the particle along the direction of relative motion ($C_D = 2F_D/(\pi a^2 \rho_c U_\infty^2)$). U_∞ is the relative velocity of the continuous phase far from the particle and a is its radius. The drag coefficient varies with the fluid particle Reynolds number $Re = 2a\rho_c U_\infty/\mu_c$ characterizing the flow in the continuous phase. ρ_c and μ_c are the density and dynamic viscosity of the fluid forming the continuous phase, respectively, whereas ρ_d and μ_d denote the corresponding quantities in the dispersed phase. The quantity κ in (1) is the viscosity ratio $\kappa = \mu_d\mu_c$.

The limiting case of a rigid particle is obtained when $\theta_{cap} = 0$ and $\kappa \to \infty$, and the corresponding drag coefficient is denoted C_D^{rigid}. The effect of contamination of the interface is cancelled when $\theta_{cap} = \pi$, and the corresponding drag coefficient is denoted C_D^{mobile}. Following Sadhal and Johnson (1983), the normalized drag coefficient is introduced

$$C_D^* = \frac{C_D - C_D^{mobile}}{C_D^{rigid} - C_D^{mobile}} = \frac{1}{2\pi}\left(2(\pi-\theta_{cap})+\sin(\theta_{cap})+\sin(2\theta_{cap})-\frac{1}{3}\sin(3\theta_{cap})\right). \quad (2)$$

An analytical solution is found for $Re \to 0$ because the non-linear inertia terms in the Navier–Stokes equations vanish. The analytical solution of Sadhal and Johnson (1983) recovers the steady creeping flow solution past a rigid sphere first determined by Stokes (1851)

* Corresponding author.
E-mail address: abdellah.saboni@univ-pau.fr (A. Saboni).

0301-9322/$ - see front matter © 2010 Elsevier Ltd. All rights reserved.
doi:10.1016/j.ijmultiphaseflow.2010.01.009

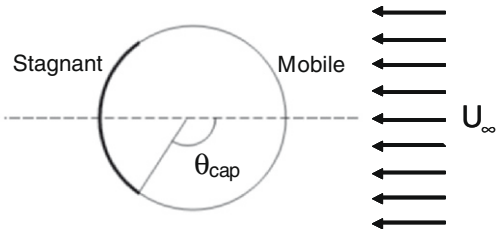

Fig. 1. Stagnant cap model.

$$C_D = \frac{24}{\mathrm{Re}}, \tag{3}$$

and the Hadamard (1911) and Rybczynski (1911) solution for steady creeping flow past a fluid sphere

$$C_D = \frac{8}{\mathrm{Re}}\left(\frac{2+3\kappa}{1+\kappa}\right). \tag{4}$$

The creeping flow solution is only valid for an asymptotically small Reynolds number, a condition which is in general admitted to correspond to $Re < 0.1$. This paper presents the results of a numerical study aimed at considering the effect of contamination on the drag coefficient applied on bubbles or drops for a higher Reynolds range $Re < 400$. This upper limit was chosen, considering that flow is eventually non-axisymmetric around a rigid sphere at a higher Reynolds number, or that the shape of an air bubble in water is no longer quasi-spherical. This numerical study solves the Navier–Stokes equations inside and outside a contaminated fluid sphere.

Ignoring the effect of contamination of the interface of a bubble or a drop, many experimental and theoretical works have been reported in the literature concerning the characteristics of flow past a bubble, a drop or a rigid sphere, with Reynolds numbers higher than in the creeping flow case.

In the case of a rigid particle, this was considered in particular by Rimon and Cheng (1969), Leclair et al. (1970), Dennis and Walker (1971), Magnaudet et al. (1995), Alassar et al. (1999), Feng and Michaelides (2001) and Saboni et al. (2004). The empirical correlation of Clift et al. (1978),

$$C_D = \frac{24}{Re}(1 + 0.15Re^{0.687}), \tag{5}$$

commonly used in practical calculations involving rigid particles, coincides with the numerical results obtained by Magnaudet et al. (1995) with an error less than 6%.

For a fluid particle with a non-contaminated interface, the case $\kappa = 0$, which corresponds to viscous flow around a spherical bubble, was studied by several authors (Brabston and Keller, 1975; Ryskin and Leal, 1984; Magnaudet et al., 1995; Blanco and Magnaudet, 1995; Raymond, 1995; Saboni et al., 2004). The boundary layer approximation used by Moore (1963) leads to

$$C_D = \frac{48}{Re}\left(1 - 2.21Re^{-\frac{1}{2}}\right). \tag{6}$$

The drag values given by this formula coincide very well with those calculated numerically by Magnaudet et al. (1995) for $Re > 50$. For $Re < 50$, a correlation based on the best fitting of these numerical results was proposed by Magnaudet et al. (1995)

$$C_D = \frac{16}{Re}\left(1 + 0.15Re^{\frac{1}{2}}\right). \tag{7}$$

Solving the Navier–Stokes equations for intermediate viscosity ratios requires solving the coupled flows inside and outside the fluid sphere, and because of this only a few works have been published. Dispersed systems with intermediate viscosity ratios are usually found in industrial processes: an example is liquid–liquid extraction, in which the viscosity ratio may vary between 0.05 and 10.

Abdel-Alim and Hamielec (1975) used a finite-difference method to calculate steady motion for $Re \leqslant 50$ and a viscosity ratio $\kappa \leqslant 1.4$. This work was extended to higher Reynolds numbers (up to 200) by Rivkind and Ryskin (1976) and Rivkind et al. (1976). Oliver and Chung (1987) used a different method (series truncation with a cubic finite-element method) for moderate Reynolds numbers $Re \leqslant 50$. Dandy and Leal (1989) studied numerically the buoyancy driven motion of a deformable drop in an unbounded fluid for $Re \leqslant 300$. Feng and Michaelides (2001), Saboni and Alexandrova (2002) and Saboni et al. (2004) used a finite-difference method to calculate the flow field inside and outside the fluid sphere. The results provide information on the two-flow field and values for the drag coefficients of viscous spheres over the entire viscosity ratio range. Saboni et al. (2004) proposed a predictive equation for drag coefficients covering Reynolds numbers in the range $0.01 \leqslant Re \leqslant 400$ and viscosity ratios from 0 to 1000.

The effect of contamination of the interface was investigated for higher Reynolds numbers by Cuenot et al. (1997), considering the transient change in flow around a spherical bubble rising in a liquid contaminated by a weakly soluble surfactant. The results confirm the validity of the stagnant-cap model for describing flow around a bubble contaminated by slightly soluble surfactants. McLaughlin (1996) considered the effect of an insoluble surfactant on flow around a deforming bubble. The stagnant-cap model was also used to perform numerical simulations of mass transfer around a bubble in the presence of surfactants in the liquid phase (Ponoth and McLaughlin, 2000; Vasconcelos et al., 2002; Dani, 2007; Madhavi et al., 2007).

Recent numerical and theoretical studies have investigated of the instability of uniform flow past a sphere (Kim and Pearlstein, 1990; Natarajan and Acrivos, 1993; Johnson and Patel, 1999). The flow becomes non-axisymmetric around $Re_{c1} = 210$ but remains steady. The transition to the 3D unsteady periodic regime is reached at a critical Reynolds number $Re_{c2} = 272$ (Natarajan and Acrivos, 1993; Johnson and Patel, 1999). For $Re > 200$, the 3D numerical simulations give more precise results (and details of the flow) than the forced axisymmetric flow. However the changes in the drag coefficient are not important. For instance, the 3D numerical results of Johnson and Patel (1999) gives a value for CD of 0.656 at $Re = 300$ with an oscillation amplitude of 3.5×10^{-3}. Tomboulides (1993) found CD = 0.671 with an oscillation amplitude of 2.8×10^{-3}, while the experimental data of Roos and Willmarth gives an interpolated value for CD of 0.629 at $Re = 300$. These values are close to those obtained from the 2D simulations which are included between 0.63 and 0.65 (Leclair et al., 1970; Magnaudet et al., 1995; Feng and Michaelides, 2001; Saboni et al., 2004).

The bubbles rising trajectories are much dependent on the bubble size and on the properties of the liquid (Clift et al., 1978). For example, in a pure water system, bubbles following a rectilinear path change to follow a zigzag path when their equivalent

Table 1
Comparison of the present results for drag coefficient with the Sadhal and Johnson analytical solution for $Re = 0.1$ and different viscosity ratios (1: Sadhal & Johnson, 2: Present results).

θ_{cap}	$\kappa = 0$		$\kappa = 1$		$\kappa = 10$	
	1	2	1	2	1	2
0	240–00	244.55	240.00	246.89	240.00	242.44
64	233.91	237.96	236.95	243.03	239.94	241.60
90	216.97	220.24	228.48	233.13	239.79	239.97
124	182.76	185.20	211.24	215.51	239.44	236.62
180	160.00	161.99	200.00	205.55	239.20	235.16

Table 2
Comparison of the present results for drag coefficient with other numerical works in the case of a bubble ($k = 0$).

Re	θ_{cap}	Cuenot et al. (1997)	Takemura and Yabe (1999)	Sarrot (2006)	Dani (2007)	Present results
10	0	–	4.22	4.33	4.33	4.42
	64	–	4.19	–	4.32	4.33
	90	–	3.76	3.80	3.81	3.86
	124	–	2.88	–	2.91	2.92
	180	–	2.37	2.43	2.44	2.47
100	0	1.09	1.09	1.10	1.09	1.09
	64	–	1.02	–	1.07	1.07
	90	0.91	0.83	0.89	0.85	0.88
	124	–	0.51	–	0.52	0.50
	180	0.37	0.38	0.37	0.38	0.37

diameter exceeds 1.8 mm ($Re \sim 600$) (Duineveld, 1995). However, a slight contamination of the water may critically affect the behavior of the bubbles and dramatically lower the Reynolds number at which a zigzag trajectory is produced.

The paper presents the results of a parametric numerical study in which the drag coefficients applied to a spherical fluid volume in steady motion were computed over the ranges $0.1 < Re < 400$ and $0 < \kappa < 10$ for seven different values of the polar angle θ_{cap} characterizing the extent of the rigid cap at the rear of the bubble or drop ($\theta_{cap} = 0°$, 30°, 64°, 90°, 124°, 150° and 180°). The paper is divided up as follows. The governing equations and the method of solution are described in Sections 2 and 3 presents the results of the numerical computations. For $Re = 0.1$, the drag coefficient values computed by our model are first compared with the analytical results

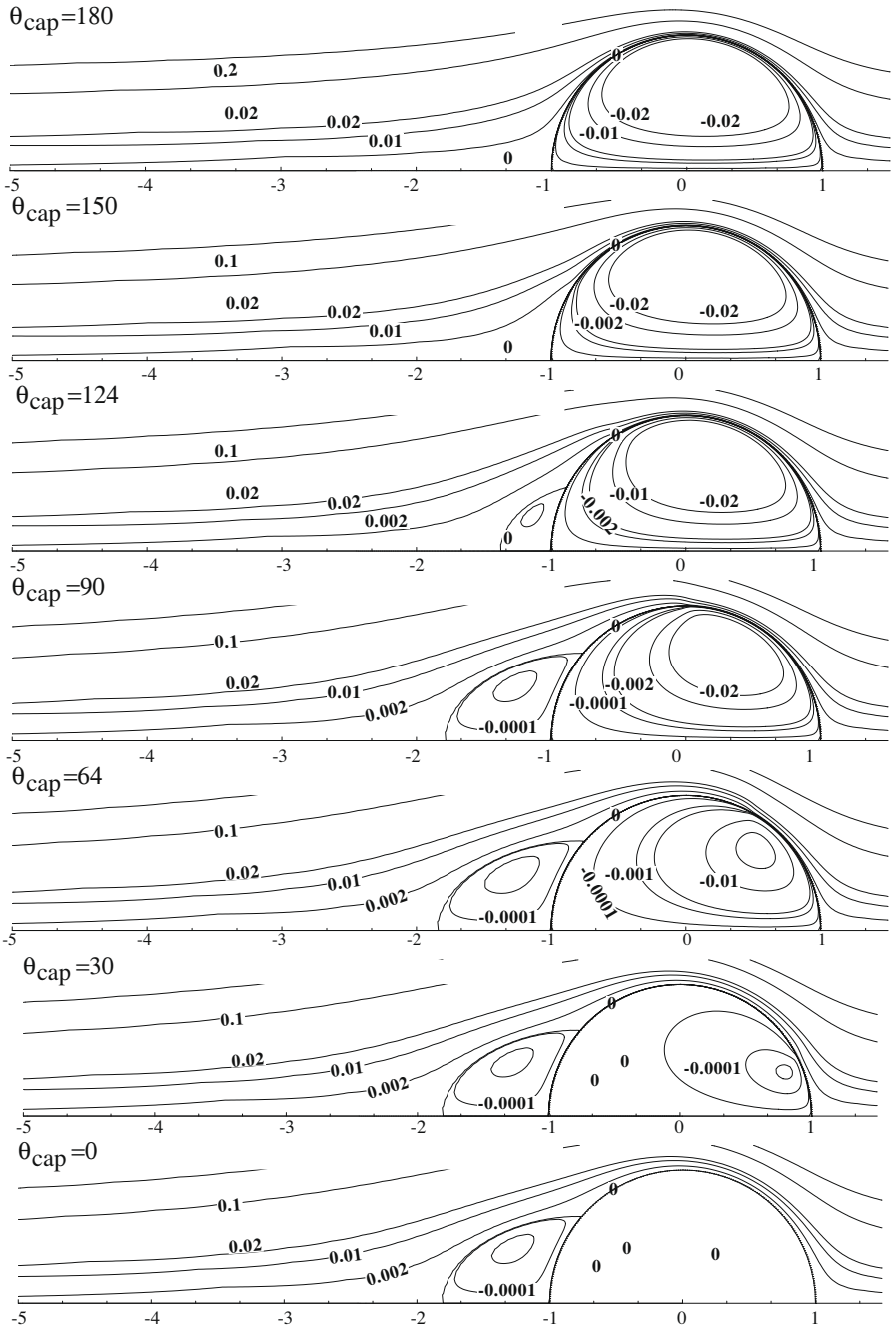

Fig. 2. Stream function contours, inside and outside a fluid sphere for $Re = 50$, $\kappa = 1$, and different stagnant caps.

of Sadhal and Johnson (1983). The results obtained for higher Reynolds numbers (up to $Re = 400$) are then analyzed in terms of maps of the stream function contours inside and outside the fluid particle, and in terms of variations in the tangential velocity and vorticity at the surface of the sphere. Lastly, the dependence of the drag coefficient on the polar angle θ_{cap} of the rigid cap is discussed using the normalized drag coefficient C_D^* (Eq. (2)) introduced by Sadhal and Johnson (1983) with the drag coefficient C_D^{mobile} given by Saboni et al. (2004) for a non-contaminated fluid particle

$$C_D^{mobile} = \frac{\left(\kappa\left(\frac{24}{Re}+\frac{4}{Re^{0.36}}\right)+\frac{15}{Re^{0.82}}-0.02\frac{\kappa Re^{0.5}}{1+\kappa}\right)Re^2+40\frac{3\kappa+2}{Re}+15\kappa+10}{(1+\kappa)(5+0.95Re^2)}, \tag{8}$$

and the drag coefficient C_D^{rigid} deduced from this formula for an asymptotically large value of κ, i.e.

$$C_D^{rigid} = \frac{24Re^2+4Re^{2.64}+15Re+120}{Re(5+0.95Re^2)}. \tag{9}$$

2. Governing equations

Consider a contaminated fluid sphere of radius a moving with uniform velocity U_∞ in another immiscible fluid of infinite extent. The kinematic viscosity is denoted ν, using subscripts d and c to refer to the dispersed and continuous phases, respectively. The Reynolds number $Re = 2aU_\infty/\nu_c$ is sufficiently low to assume that the

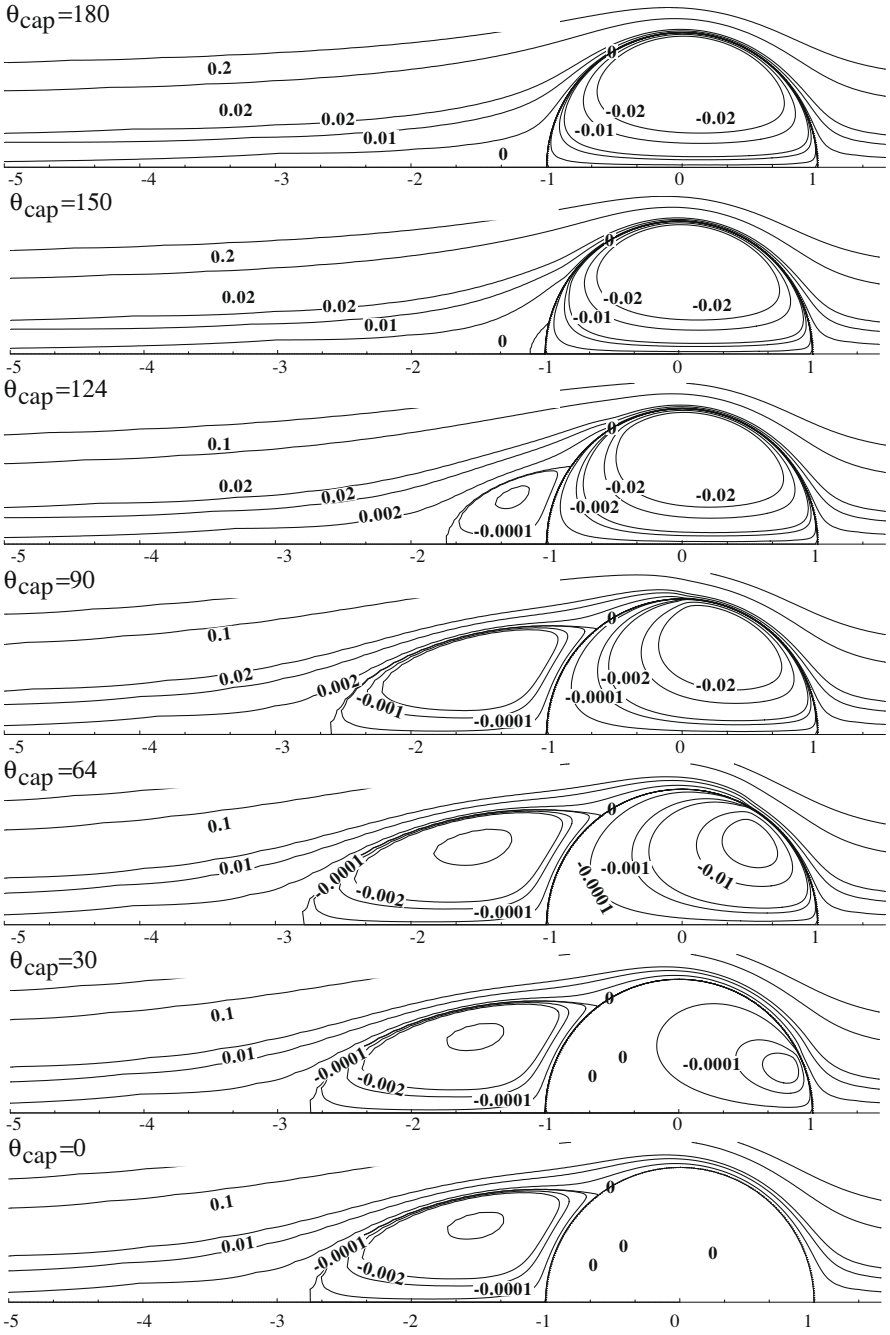

Fig. 3. Stream function contours, inside and outside a fluid sphere for $Re = 100$, $\kappa = 1$, and different stagnant caps.

flow is axisymmetric in the two phases, and the Navier–Stokes equations are written in terms of the stream function and vorticity (ψ and ω) in the r and θ spherical coordinates system (Clift et al., 1978; Sadhal et al., 1996).

Inside the spherical fluid particle (dispersed phase), the equations to be solved are

$$E^2\psi_d = \omega_d r\sin\theta, \tag{10}$$

$$\frac{\mu_c}{\mu_d}\frac{\rho_d}{\rho_c}\frac{\mathrm{Re}}{2}\left[\frac{\partial\psi_d}{\partial r}\frac{\partial}{\partial\theta}\left(\frac{\omega_d}{r\sin\theta}\right)-\frac{\partial\psi_d}{\partial\theta}\frac{\partial}{\partial r}\left(\frac{\omega_d}{r\sin\theta}\right)\right]\sin\theta = E^2(\omega_d r\sin\theta), \tag{11}$$

where $E^2 = \frac{\partial^2}{\partial r^2}+\frac{\sin\theta}{r^2}\frac{\partial}{\partial\theta}\left(\frac{1}{\sin\theta}\frac{\partial}{\partial\theta}\right)$.

Outside the fluid sphere, the radial coordinate r is transformed for numerical reasons, introducing the logarithmic radial coordinate z ($r = ez$). The above set of equations is modified to

$$E^2\psi_c = \omega_c e^z\sin\theta, \tag{12}$$

$$\frac{Re}{2}\left[\frac{\partial\psi_c}{\partial z}\frac{\partial}{\partial\theta}\left(\frac{\omega_c}{e^z\sin\theta}\right)-\frac{\partial\psi_c}{\partial\theta}\frac{\partial}{\partial z}\left(\frac{\omega_c}{e^z\sin\theta}\right)\right]e^z\sin\theta = e^{2z}E^2(\omega_c e^z\sin\theta). \tag{13}$$

The dimensionless quantities are related to the dimensional variables (denoted with a prime) by $r = r'/a$, $\omega = \omega' a/U^\infty$ and $\psi = \psi'/(U^\infty a2)$.

The dimensionless radial and tangential velocities are determined from the dimensionless stream function ψ by

$$u = -\frac{1}{r^2\sin\theta}\frac{\partial\psi}{\partial\theta};\quad v = \frac{1}{r\sin\theta}\frac{\partial\psi}{\partial r}. \tag{14}$$

The two systems of equations are solved in the continuous and dispersed phases. The effect of interface contamination is taken into

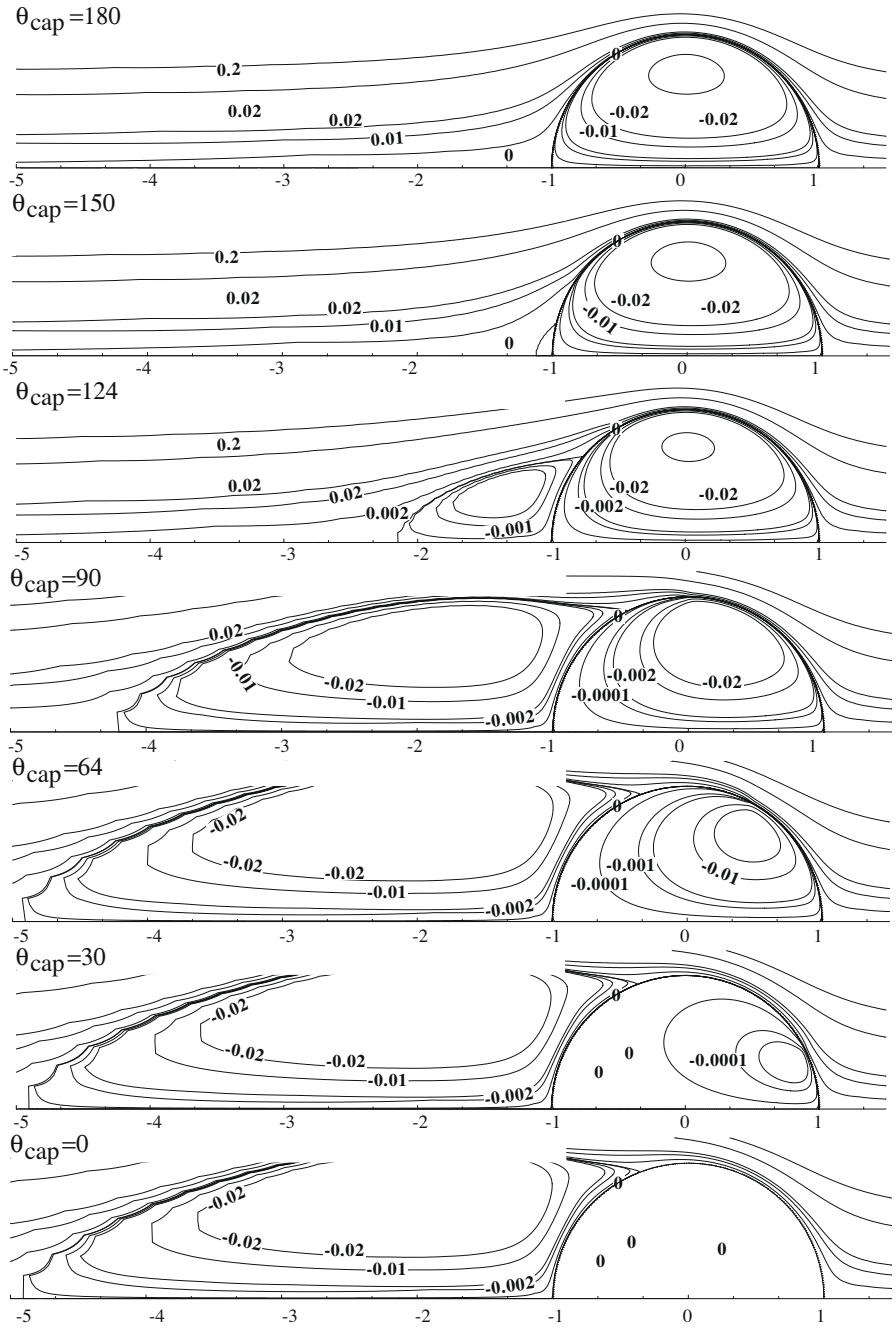

Fig. 4. Stream function contours, inside and outside a fluid sphere for $Re = 300$, $\kappa = 1$, and different stagnant caps.

account solely by the value of the polar angle θ_{cap} of the rigid cap at the rear of the particle through the associated boundary conditions:

(i) Far from the fluid sphere ($z = z^{\infty}$), undisturbed parallel flow is assumed: $\omega_c = 0$; $\psi_c = 0.5e^{2z}\sin^2\theta$.

(ii) Along the axis of symmetry ($\theta = 0, \pi$): $\psi_c = 0$, $\omega_c = 0$, $\psi_d = 0$, $\omega_d = 0$.

(iii) Across the mobile part of the interface ($\theta < \theta_{cap}$ and $z = 0$ or $r = 1$), the following relations express, respectively, negligible material transfer, continuity of the tangential velocity, and continuity of the tangential stress

$$\psi_c = 0; \quad \psi_d = 0; \quad \frac{\partial \psi_c}{\partial z} = \frac{\partial \psi_d}{\partial r};$$

$$\frac{\mu_c}{\mu_d}\left(\frac{\partial^2 \psi_c}{\partial z^2} - 3\frac{\partial \psi_c}{\partial z}\right) = \left(\frac{\partial^2 \psi_d}{\partial r^2} - 2\frac{\partial \psi_d}{\partial r}\right).$$

(iv) On the surface of the rigid cap ($\theta > \theta_{cap}$ and $z = 0$ or $r = 1$), and the tangential velocity is zero

$$\psi_c = 0; \quad \psi_d = 0; \quad \frac{\partial \psi_c}{\partial z} = \frac{\partial \psi_d}{\partial r} = 0$$

Eqs. (10)–(13) subjected to the boundary conditions (i)–(iv) are solved simultaneously to obtain stream-function and vorticity values. Once stream function is known, the velocities are then determined from (14).

The finite-difference method is used in the present study. While detailed discussions on the accuracy of the solution procedure employed are available elsewhere (Saboni et al., 2004; Saboni et al., 2007), the reliability and accuracy of the diffusion–convection equation for the solution is established here by comparing the present values with the literature values in the case of a spherical contaminated bubble.

3. Results and discussion

The method of solution is first tested by considering the limiting case of a bubble ($\kappa = 0$). Computations of the drag coefficient are compared in Table 1 with the Sadhal & Johnson analytical solution. In the case of the different stagnant cap angles ($\theta_{cap} = 180°$, 124°, 90°, 64° and 0), it shows good agreement between our results and the creeping flow analytical solution ($Re = 0.1$). The case $\theta_{cap} = 180°$ corresponds to uniform flow past a sphere with fully mobile interface (air bubble in water). The values of the drag coefficient computed are in good agreement with those of Brabston and Keller (1975) and Ryskin and Leal (1984). The case $\theta_{cap} = 0$ corresponds to uniform flow past a rigid sphere with an immobile interface. Our results agree well with those of Leclair et al. (1970), Alassar et al. (1999) and Feng and Michaelides (2001).

In the case of the bubble ($\kappa = 0$) and higher Reynolds numbers, the drag coefficients computed by our numerical model are compared in Table 2 with the results of Cuenot et al. (1997), Takemura and Yabe (1999), Sarrot (2006) and Dani (2007). Good agreement is found for the two Reynolds numbers considered ($Re = 10$ and $Re = 100$) and the different stagnant cap angles ($\theta_{cap} = 180°$, 124°, 90°, 64° and 0). An analysis of Table 2 indicates in a qualitative manner that the variation in drag coefficient with the polar angle θ_{cap} of the spherical cap occurs mainly when this angle is between 64° and 124°. When $0 < \theta_{cap} < 64°$, the drag coefficient remains approximately the same as in the case of the rigid sphere. Similarly, the drag coefficient for non-contaminated conditions is approximately recovered for $124° < \theta_{cap} < 180°$.

This qualitative interpretation of drag coefficient variations is illustrated in Fig. 2, which shows streamline contours inside and outside a fluid sphere for $Re = 50$, $\kappa = 1$ and the different stagnant cap angles. At high stagnant cap angles ($\theta_{cap} = 180°$ and 124°), it appears that internal circulation is sufficiently rapid to prevent flow separation and the formation of a trailing vortex. Slight asymmetry is observed between upstream and downstream regions near the sphere. With low stagnant cap angles the contour line plots show flow separation downstream of the fluid particle, which is very similar in all cases with $0 < \theta_{cap} < 90°$. The effect of the angle θ_{cap} characterizing the degree of contamination concerns mainly flow inside the fluid particle, which has a limited effect on the drag coefficient. Similar conclusions are obtained for the two Reynolds numbers $Re = 100$ and 300 (and $\kappa = 1$) as shown in Figs. 3 and 4 for different stagnant cap angles ($\theta_{cap} = 180$, 150, 124, 90, 64, 30 and 0). Here also, a slight asymmetry about $\theta = 90$ is seen with high

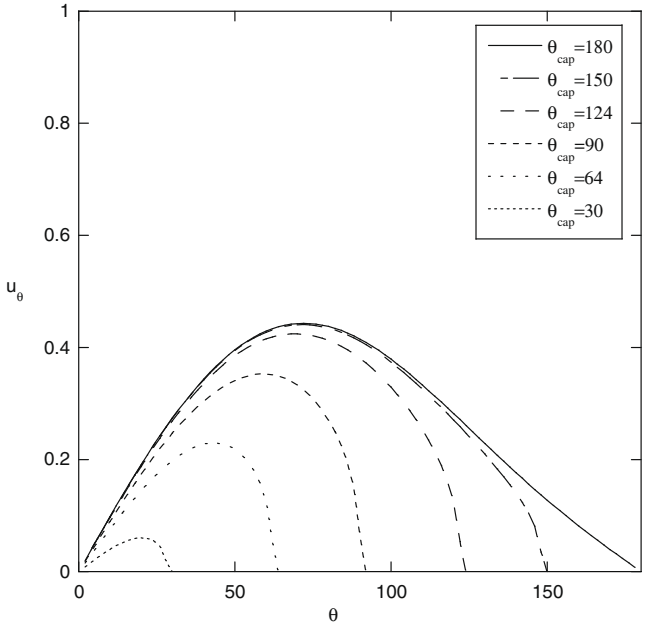

Fig. 5. Tangential velocity distribution at surface of sphere for $Re = 10$, and different stagnant caps.

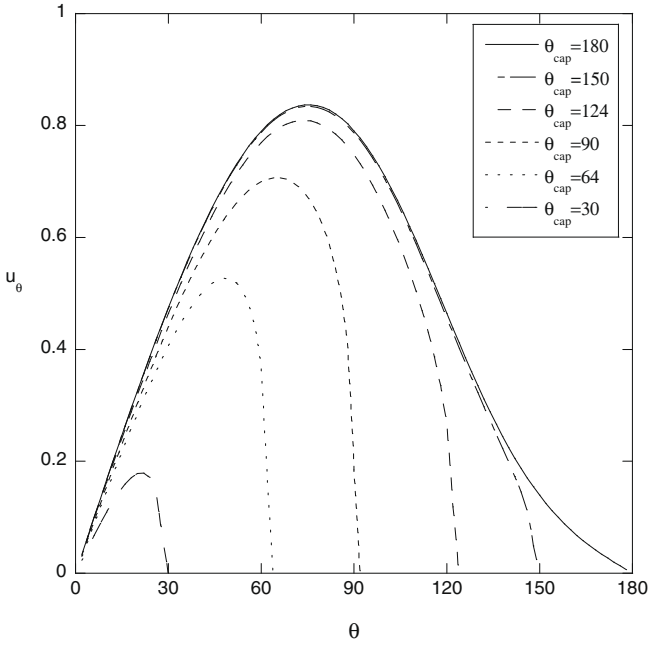

Fig. 6. Tangential velocity distribution at surface of sphere for $Re = 100$, and different stagnant caps.

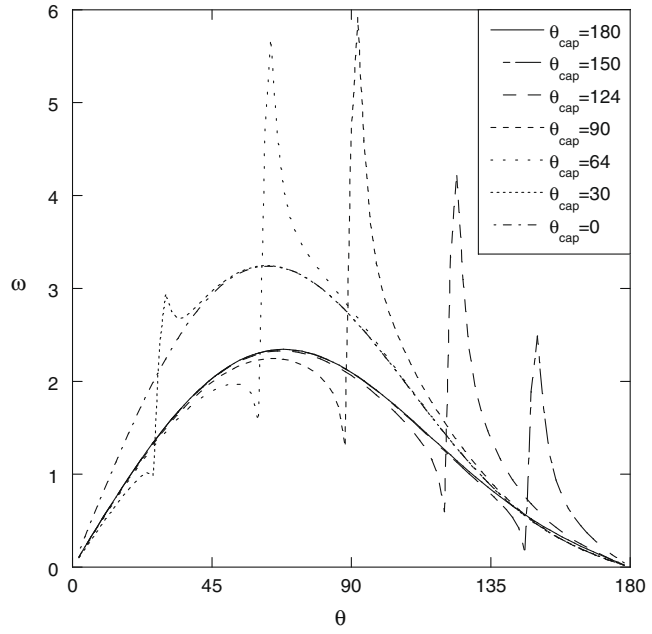

Fig. 7. Vorticity distribution at surface of sphere for $Re = 10$ and different stagnant caps.

stagnant cap angles. In Figs. 2–4, it may be seen that the eddy length and the angle of flow separation increase with decreasing stagnant cap angle.

The tangential velocity u_θ at the surface of a moving contaminated fluid sphere ($k = 1$) is plotted in Figs. 5 and 6 (for $Re = 10$ and 100, respectively) as a function of the angular coordinate θ for different stagnant cap angles ($\theta_{cap} = 180$, 150, 124, 90, 64, 30 and 0). With an uncontaminated fluid sphere ($\theta_{cap} = 180$), the velocity is positive and reaches its maximum near the equator. When a portion of the sphere interface is contaminated, the speed is almost unchanged upstream of the rigid cap but it decreases suddenly when approaching it. This sudden change is illustrated in a complementary manner in Figs. 7 and 8, where the variation in vorticity ω at the surface of the moving contaminated fluid sphere is plotted for the different stagnant cap angles with the two Reynolds numbers $Re = 10$ and $Re = 100$ (and $\kappa = 1$). The limiting profiles for a fully contaminated sphere ($\theta_{cap} = 0$) and non-contaminated sphere ($\theta_{cap} = 180$) deserve particular attention because the vorticity variations for the intermediate angles $0 < \theta_{cap} < 180$ are attached to them. With $Re = 10$, the vorticity variations look similar for $\theta_{cap} = 0$ and $\theta_{cap} = 180$, with a maximum vorticity around $\theta = 60$, but the vorticity is higher on the rigid sphere ($\theta_{cap} = 0$) than on the non-contaminated sphere ($\theta_{cap} = 180$). At a higher Reynolds number ($Re = 100$, Fig. 8), the vorticity is negative at the rear of the rigid sphere ($\theta_{cap} = 0$), indicating recirculation behind the sphere, as observed in Fig. 3. No circulation behind the sphere is found for $Re = 10$. These results are in agreement with the literature dealing with rigid and fluid spheres. In intermediate cases ($\theta_{cap} = 150$, 124, 90, 64, 30), it can be seen that the vorticity profile is similar to that of a rigid sphere on the contaminated part, and close to that of a fluid sphere on the non-contaminated part. The vorticity exhibits a very sharp peak at the transition between the contaminated and non-contaminated parts of the sphere.

Table 3 summarizes the values of the drag coefficient C_d obtained from our calculations for the range of parameters covered ($Re = 10$–400, $\kappa = 0.5$–10) and the different stagnant cap angles

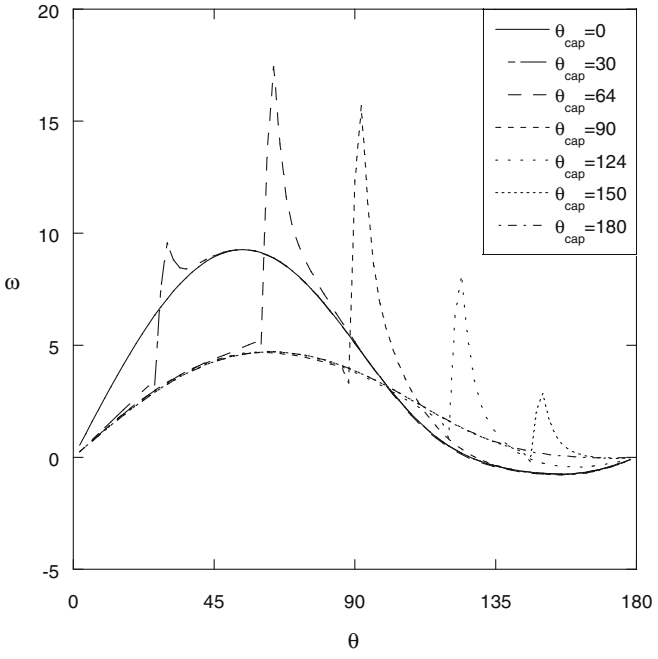

Fig. 8. Vorticity distribution at surface of sphere for $Re = 100$ and different stagnant caps.

Table 3
Effect of interface contamination on a fluid sphere drag coefficient.

Re	θ_{cap}						
	0	30	64	90	124	150	180
κ = 0.5							
10	4.42	4.42	4.36	4.05	3.43	3.13	3.07
20	2.78	2.77	2.75	2.51	2.07	1.87	1.94
50	1.59	1.59	1.58	1.41	1.07	0.95	0.93
100	1.09	1.09	1.08	0.94	0.66	0.59	0.55
200	0.77	0.77	0.75	0.63	0.40	0.32	0.31
300	0.62	0.62	0.60	0.48	0.30	0.23	0.22
400	0.53	0.53	0.50	0.40	0.24	0.18	0.18
κ = 1							
10	4.42	4.42	4.38	4.14	3.69	3.46	3.41
20	2.78	2.78	2.75	2.58	2.24	2.09	2.09
50	1.59	1.59	1.59	1.45	1.20	1.10	1.09
100	1.09	1.09	1.09	0.97	0.74	0.67	0.66
200	0.77	0.77	0.75	0.65	0.46	0.4	0.39
300	0.62	0.62	0.60	0.51	0.34	0.29	0.28
400	0.53	0.53	0.50	0.42	0.28	0.23	0.23
κ = 2							
10	4.42	4.42	4.40	4.24	3.94	3.80	3.76
20	2.78	2.75	2.74	2.62	2.41	2.31	2.30
50	1.59	1.59	1.59	1.50	1.33	1.27	1.26
100	1.09	1.09	1.09	1.01	0.86	0.81	0.81
200	0.77	0.77	0.77	0.69	0.55	0.51	0.50
300	0.62	0.62	0.61	0.54	0.42	0.38	0.37
400	0.53	0.53	0.51	0.45	0.34	0.31	0.30
κ = 3							
10	4.42	4.42	4.40	4.28	4.06	3.95	3.93
20	2.78	2.77	2.76	2.68	2.51	2.44	2.43
50	1.59	1.59	1.59	1.53	1.40	1.35	1.35
100	1.09	1.09	1.09	1.04	0.92	0.89	0.88
200	0.77	0.77	0.77	0.71	0.60	0.58	0.57
300	0.62	0.62	0.62	0.56	0.46	0.44	0.44
400	0.53	0.53	0.53	0.47	0.38	0.36	0.36
κ = 10							
10	4.42	4.42	4.40	4.34	4.26	4.22	4.22
20	2.78	2.78	2.78	2.75	2.69	2.67	2.67
50	1.59	1.59	1.59	1.58	1.53	1.51	1.51
100	1.09	1.09	1.09	1.08	1.04	1.03	1.03
200	0.77	0.77	0.77	0.76	0.72	0.71	0.71
300	0.62	0.62	0.62	0.61	0.57	0.57	0.57
400	0.53	0.53	0.53	0.52	0.49	0.48	0.48

(θ_{cap} = 180, 150, 124, 90, 64, 30 and 0). As expected, the drag coefficient decreases with increasing Reynolds numbers for a fixed stagnant cap angle and a given viscosity ratio κ. With a fixed Reynolds number, the drag coefficient also decreases for an increasing stagnant cap angle. The values for $\theta_{cap} = 180$ and $\theta_{cap} = 0$ coincide with the drag coefficient for a rigid sphere and a clean fluid sphere, respectively. Table 3 quantifies the qualitative observations on Figs. 2–4 that the effect of contamination is mainly significant when the cap angle θ_{cap} is between 64° and 124°. Indeed, the drag coefficient is approximately the same as for the rigid sphere with $\theta_{cap} < 64°$ and only a limited decrease is noticed for $\theta_{cap} = 90°$. The values are almost independent of the viscosity ratio κ. It can also be seen that the drag coefficient is approximately the same with $\theta_{cap} = 150°$ and 180°. Increasing the viscosity ratio κ is associated with an increase in the drag coefficient, as observed in the case of a non-contaminated fluid sphere.

Because the rigid sphere ($\theta_{cap} = 0$) and the non-contaminated fluid sphere ($\theta_{cap} = 180$) cases are the reference limit cases from which the drag coefficient deviates in the intermediate range of cap angle θ_{cap} characterizing the degree of contamination of the interface, the variations in drag coefficient C_D^* with θ_{cap} were considered. They are plotted in Fig. 9 for four different values of the Reynolds number and varying viscosity ratios. On each figure the variations with θ_{cap} derived analytically by Sadhal and Johnson (1983) for an asymptotically low Reynolds number ($Re \to 0$) are superimposed. As a result of definition the normalized drag coefficient is equal to unity for a completely contaminated fluid sphere ($\theta_{cap} = 0$) and to zero for a non-contaminated fluid sphere ($\theta_{cap} = 180$). While our computations closely reproduce the Sadhal and Johnson solution at low Reynolds numbers $Re = 0.1$ and $Re = 10$, Fig. 9 shows that the variations in normalized drag coefficient with θ_{cap} deviate increasingly from the Sadhal and Johnson curve as the Reynolds number or viscosity ratio are increased. The difference between C_D^{mobile} and C_D^{rigid} is reduced as much as the viscosity ratio is increased (Table 3), and this explains the scatter observed in Fig. 9 when using a normalized C_D^*.

The differences between the non-normalized C_D obtained from our computations and the C_D obtained using the Sadhal and Johnson C_D^*, i.e.

$$C_D = C^*_{D,Sadhal\&Johnson}\left(C_D^{rigid} - C_D^{mobile}\right) + C_D^{mobile}, \tag{14}$$

are much less pronounced. As an example with $Re = 400$, $\kappa = 3$ and $\theta_{cap} = 124$, the Sadhal and Johnson C_D^* and the numerical C_D^* are respectively 0.284 and 0.117 while the C_D given by (14) and the numerical C_D are respectively 0.36 and 0.38. Tables 4 and 5 show that the results from Eq. (14) agree well with those obtained numerically. The cases $Re = 10$ and 300 are given as an example but it is very easy to confirm these observations with any other value $Re < 400$. Values of the drag coefficient given by this formula coincide with those calculated numerically with an error of less than 15% over the entire range of Re, κ and θ_{cap} covered by our investigation ($0 < Re < 400$, $0 < \kappa < 10$ and $0 < \theta_{cap} < 180$). It may therefore be suggested that Eq. (14) should be used to determine the drag coefficient for a contaminated fluid sphere in the case of Reynolds numbers ranging between 0.01 and 400 and viscosity ratios between 0 and 10.

Our simulations assume that the particle is spherical. The applicability of the present correlation relies on the validity of this hypothesis. Clift et al. proposed a general graph (based on the values of Bond, Morton, and Reynolds numbers) which predicts the shape of bubbles and drops. The graph shows that the falling or rising bubble or drop will remain spherical for $Re < 1000$ when the Bond number Bo is less than 0.3. Such condition is met for bubbles

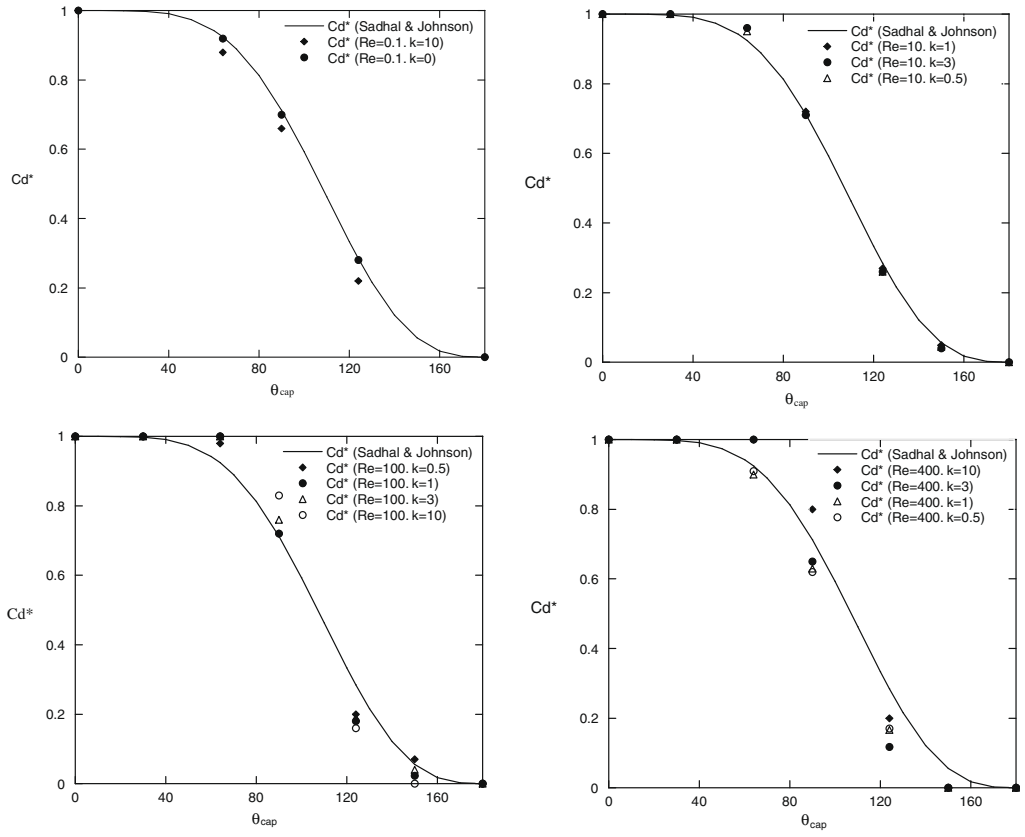

Fig. 9. Normalized drag coefficient Cd of a fluid sphere versus cap angle θ_{cap} plotted for different Reynolds numbers $Re = 0.1$, 10, 100 and 400 and varying viscosity ratios κ. The solid curve is the analytical solution by Sadhal and Johnson (1983) for an asymptotically low Reynolds number ($Re \to 0$).

Table 4
Comparison of the present numerical results for C_d with the results from Eq. (14) for $Re = 10$.

κ	θ_{cap}						
	0	30	64	90	124	150	180
0.5							
Present numerical results	4.42	4.42	4.36	4.05	3.43	3.13	3.07
Eq. (14)	4.42	4.41	4.31	4.03	3.46	3.16	3.09
1							
Present numerical results	4.42	4.42	4.36	4.14	3.69	3.46	3.41
Eq. (14)	4.42	4.41	4.34	4.18	3.70	3.47	3.42
2							
Present numerical results	4.42	4.42	4.40	4.24	3.94	3.80	3.76
Eq. (14)	4.41	4.41	4.36	4.22	3.93	3.78	3.74
3							
Present numerical results	4.42	4.42	4.40	4.28	4.06	3.95	3.93
Eq. (14)	4.42	4.41	4.37	4.27	4.05	3.94	3.91
10							
Present numerical results	4.42	4.42	4.40	4.34	4.26	4.22	4.22
Eq. (14)	4.42	4.41	4.40	4.36	4.28	4.24	4.23

Table 5
Comparison of the present numerical results for C_d with the results from Eq. (14) for $Re = 300$.

κ	θ_{cap}						
	0	30	64	90	124	150	180
0.5							
Present numerical results	0.62	0.62	0.60	0.48	0.30	0.23	0.22
Eq. (14)	0.62	0.62	0.59	0.51	0.34	0.25	0.23
1							
Present numerical results	0.62	0.62	0.60	0.51	0.34	0.29	0.28
Eq. (14)	0.62	0.62	0.60	0.53	0.39	0.31	0.29
2							
Present numerical results	0.62	0.62	0.61	0.54	0.42	0.38	0.38
Eq. (14)	0.62	0.62	0.60	0.55	0.45	0.39	0.38
3							
Present numerical results	0.62	0.62	0.62	0.56	0.46	0.44	0.44
Eq. (14)	0.62	0.62	0.61	0.57	0.49	0.45	0.43
10							
Present numerical results	0.62	0.62	0.62	0.61	0.57	0.57	0.57
Eq. (14)	0.62	0.62	0.62	0.60	0.57	0.55	0.55

with $Re < 300$. For $Re < 100$ and $We < 0.5$ (slightly deformed particle) the correlation values of the drag coefficient given by the Eq. (8) coincide with those calculated numerically by Dandy and Leal (with an error of less than 10%).

The correlation presented in this paper is precise in the absence of instability ($Re < 200$). Its precision for $Re > 200$ should be checked by 3D computations of unsteady non-axisymmetric flow.

4. Conclusions

A numerical study has been conducted to investigate the effects of contamination on flow around a fluid sphere. This paper presents the results of a parametric numerical study in which the drag coefficients applied to a spherical fluid volume in steady motion were computed over the ranges $0.1 < Re < 400$ and $0 < \kappa < 10$ for seven different values of the polar angle θ_{cap} characterizing the extent of a rigid cap at the rear of the bubble or drop ($\theta_{cap} = 0°$, 30°, 64°, 90°, 124°, 150° and 180°). The results show that the flow is strongly dependent on the Reynolds number and stagnant cap angle. As expected, the drag coefficient decreases with increasing Reynolds numbers in the case of a fixed stagnant cap angle and a given viscosity ratio κ. With a fixed Reynolds number, the drag coefficient also decreases in the case of an increasing stagnant cap angle. To present the numerical results in an easier-to-use form, our numerical results are correlated by an equation based on the normalized drag coefficient derived by Sadhal and Johnson (1983) for an asymptotically low Reynolds number ($Re \to 0$) and the drag coefficients C_D^{mobile} and C_D^{rigid} given by Saboni et al. (2004) (Eqs. (8) and (9)). Values of the drag coefficient given by this formula coincide with those calculated numerically with an error less than 15% over the entire range of Re, k and θ_{cap} covered by our investigation ($0 < Re < 400$, $0 < \kappa < 10$ and $0 < \theta_{cap} < 180$).

References

Abdel-Alim, A.H., Hamielec, A.E., 1975. A theoretical and experimental investigation of the effect of internal circulation on the drag of spherical droplets falling at terminal velocity in liquid media. Ind. Eng. Chem. Fund. 14, 308–312.

Alassar, R.S., Badr, H.M., Marromatis, H.A., 1999. Heat convection from a sphere in an oscillating free stream. Int. J. Heat Mass Trans. 42 (7), 1289–1304.

Beitel, A., Heideger, W., 1971. Surfactant effects on mass transfer from drops subject to interfacial instability. Chem. Eng. Sci. 26, 711–717.

Blanco, A., Magnaudet, J., 1995. The structure of the axisymmetric high-Reynolds number flow around an ellipsoidal bubble of fixed shape. Phys. Fluids 7 (6), 1265–1274.

Brabston, D.C., Keller, H.B., 1975. Viscous flows past spherical gas bubbles. J. Fluid Mech. 69, 179–189.

Clift, R., Grace, J.R., Weber, M.E., 1978. Bubbles, Drops and Particles. Academic Press, New York.

Cuenot, B., Magnaudet, J., Spennato, B., 1997. The effects of slightly soluble surfactants on the flow around a spherical bubble. J. Fluid Mech. 339, 25–53.

Dandy, D.S., Leal, L.G., 1989. Buoyancy-driven motion of a deformable drop through a quiescent liquid at intermediate Reynolds numbers. J. Fluid Mech. 208, 161–192.

Dani, A., 2007. Transfert de masse entre une bulle et un liquide: simulations numériques directes et fluorescence induite par nappe laser. Thèse de doctorat de l'Institut National des Sciences Appliquées de Toulouse, France.

Davis, R.E., Acrivos, A., 1966. The influence of surfactants on the creeping motion of bubbles. Chem. Eng. Sci. 21, 681–685.

Dennis, S.C.R., Walker, J.D.A., 1971. Calculation of the steady flow past a sphere at low and moderate Reynolds numbers. J. Fluid Mech. 48, 771–789.

Duineveld, P.C., 1995. Rise velocity and shape of bubbles in pure water at high Reynolds number. J. Fluid Mech. 292, 325–332.

Elzinga, E., Banchero, J., 1961. Some observations on the mechanics of drops in liquid–liquid systems. AIChE J 7, 394–399.

Feng, Z.G., Michaelides, E.E., 2001. Heat and mass transfer coefficients of viscous spheres. Int. J. Heat Mass Trans. 44 (23), 4445–4454.

Garner, F.H., Skelland, A.H.P., 1955. Some factors affecting droplet behaviour in liquid–liquid systems. Chem. Eng. Sci. 4, 149–158.

Griffith, R., 1962. The effect of surfactants on the terminal velocity of drops and bubbles. Chem. Eng. Sci. 17, 1057–1070.

Hadamard, J., 1911. Mouvement permanent lent d'une sphère liquide et visqueuse dans un liquide visqueux. C. R. Acad. Sci. Paris 152, 1735–1738.

Harper, J.F., 1973. On bubbles with small immobile adsorbed film rising in liquids at low Reynolds numbers. J. Fluid Mech. 58, 539–545.

Harper, J.F., 1982. Surface activity and bubble motion. Appl. Sci. Res. 38, 343–352.

Horton, Y.J., Fritsch, I.R., Kintner, R., 1965. Experimental determination of circulation velocities inside drops. Can. J. Chem. Eng. 43, 143–146.

Huang, W., Kintner, R.C., 1969. Effects of surfactants on mass transfer inside drops. AIChE J. 15, 735–744.

Johnson, T.A., Patel, V.C., 1999. Flow past a sphere up to a Reynolds number of 300. J. Fluid Mech. 378, 19–70.

Kim, I., Pearlstein, A.J., 1990. Stability of the flow past a sphere. J. Fluid Mech. 211, 73–93.

Leclair, B.P., Hamielec, A.E., Pruppacher, H.R., 1970. A numerical study of the drag on a sphere at low and intermediate Reynolds numbers. J. Atmos. Sci. 27, 308–315.

Madhavi, T., Golder, A.K., Samanta, A.N., Ray, S., 2007. Studies on bubble dynamics with mass transfer. Chem. Eng. J. 128, 95–104.

Magnaudet, J., Rivero, M., Fabre, J., 1995. Accelerated flows past a rigid sphere or a spherical bubble. Part I: Steady straining flow. J. Fluid Mech. 284, 97–135.

McLaughlin, J.B., 1996. Numerical simulation of bubble motion in water. J. Colloid Interf. Sci. 184, 614–625.

Moore, W., 1963. The boundary layer on spherical gas bubbles. J. Fluid Mech. 16, 161.

Natarajan, R., Acrivos, A., 1993. The instability of the steady flow past spheres and disks. J. Fluid Mech. 254, 323–344.

Oliver, D.L.R., Chung, J.N., 1987. Flow about a fluid sphere at low to moderate Reynolds numbers. J. Fluid Mech. 177, 1–18.

Ponoth, S., McLaughlin, J.B., 2000. Numerical simulation of mass transfer for bubbles in water. Chem. Eng. Sci. 55, 1237–1255.

Raymond, F., 1995. Simulation numérique d'écoulements avec interfaces déformables. Thèse de doctorat de l'Ecole Centrale de Nantes, ED 82-129.

Rimon, Y., Cheng, I., 1969. Numerical solution of a uniform flow over a sphere at intermediate Reynolds number. Phys. Fluids 12, 949–965.

Rivkind, V.Y., Ryskin, G.M., 1976. Flow structure in motion of spherical drop in fluid medium at intermediate Reynolds numbers. Fluid Dyn. 11, 5–12.
Rivkind, V.Y., Ryskin, G.M., Fishben, G.A., 1976. Flow around a spherical drop at intermediate Reynolds numbers. Appl. Math. Mech. 40, 687–691.
Rybczynski, W., 1911. Uber die fortschreitende Bewegung einer flüssigen Kugel in einem zähen Medium. Bull. Polish Acad. Sci. Krakow A, 40–46.
Ryskin, G., Leal, L.G., 1984. Numerical solution of free-boundary problems in fluid mechanics. Part 1. The finite-difference technique. J. Fluid Mech. 148, 1–17.
Saboni, A., Alexandrova, S., 2002. Numerical study of the drag on a fluid sphere. AIChE J. 48 (12), 2992–2994.
Saboni, A., Alexandrova, S., Gourdon, C., 2004. Détermination de la traînée engendrée par une sphère fluide en translation. Chem. Eng. J. 98 (1-2), 175–182.
Saboni, A., Alexandrova, S., Spasic, A.M., Gourdon, C., 2007. Effect of the viscosity ratio on mass transfer from a fluid sphere at low to very high Peclet numbers. Chem. Eng. Sci. 62 (17), 4742–4750.
Sadhal, S.S., Johnson, R.E., 1983. Stokes flow past bubbles and drops partially coated with thin films – exact solution. J. Fluid Mech. 126, 237–250.
Sadhal, S.S., Ayyaswamy, P.S., Chung, J.N.C., 1996. Transport Phenomena with Drops and Bubbles. Springer, Berlin.
Sarrot, V., 2006. Capture de fines particules par des inclusions fluides. Thèse de doctorat de l'Institut National des Sciences Appliquées de Toulouse, France.
Savic, P. 1953. Circulation and distortion of liquid drops falling through a viscous medium. Tech. Rep. MT-22. Natl. Res. Counc. Can., Div. Mech. Eng.
Stokes, G.G., 1851. Trans. Cambridge Philos. Soc. 9, 8–27.
Takemura, F., Yabe, A., 1999. Rising speed and dissolution rate of a carbon dioxide bubble in slightly contaminated water. J. Fluid Mech. 378, 319–334.
Tomboulides, A.G., 1993. Direct and large-eddy simulation of wake flows: flow past a sphere. Ph.D. Dissertation, Princeton University.
Vasconcelos, J.M.T., Orvalho, S.P., Alves, S.S., 2002. Gas–liquid mass transfer to single bubbles: effect of surface contamination. AIChE J. 48 (6), 1145–1154.